

## Article

# A Novel Hydro-Thermal Synthesis of Nano-Structured Molybdenum-Iron Intermetallic Alloys at Relatively Low Temperatures

A. A. El-Geassy<sup>1</sup>, K. S. Abdel Halim<sup>2,1,\*</sup>  and Abdulaziz S. Alghamdi<sup>2</sup> 

<sup>1</sup> Central Metallurgical Research and Development Institute (CMRDI), P.O. Box 87, Helwan 11421, Egypt; elgeassy@hotmail.com

<sup>2</sup> College of Engineering, University of Ha'il, P.O. Box 2440, Hail 55476, Saudi Arabia; a.alghamdi@uoh.edu.sa

\* Correspondence: k.abdulhalem@uoh.edu.sa; Tel.: +966-531456640

**Abstract:** Nano-structured Mo/Fe intermetallics were synthesized from precursors that contained 72/28% and 30/70% molar ratios of Mo/Fe, which were given as precursors A and B, respectively. These precursors were prepared from the co-precipitation of aqueous hot solutions of ammonium heptamolybdate tetrahydrate (AHM) and ferrous oxalate. The dry precipitates were thermally treated using TG-DSC to follow up their behavior during roasting, in an Ar atmosphere of up to 700 °C (10° K/min). The TG profile showed that 32.5% and 55.5% weight losses were measured from the thermal treatment of precursors A and B, respectively. The DSC heat flow profile showed the presence of endothermic peaks at 196.9 and 392.5–400 °C during the thermal decomposition of the AHM and ferrous oxalate, respectively. The exothermic peak that was detected at 427.5 °C was due to the production of nano-sized iron molybdate [Fe<sub>2</sub>(MoO<sub>4</sub>)<sub>3</sub>]. An XRD phase analysis indicated that iron molybdate was the only phase that was identified in precursor A, while iron molybdate and Fe<sub>2</sub>O<sub>3</sub> were produced in precursor B. Compacts were made from the pressing of the nano-sized precursors, which were roasted at 500 °C for 3 h. The roasted compacts were isothermally reduced in H<sub>2</sub> at 600–850 °C using microbalance, and the O<sub>2</sub> weight loss that resulted from the reduction reactions was continuously recorded as a function of time. The influence of the reduction temperature and precursor composition on the reduction behavior of the precursors was studied and discussed. The partially and completely reduced compacts were examined with X-ray powder diffraction (XRD), a reflected light microscope (RLM), and a scanning electron microscope (SEM-EDS). Depending on the precursor composition, the reduction reactions of the [Fe<sub>2</sub>(MoO<sub>4</sub>)<sub>3</sub>] and Fe<sub>2</sub>O<sub>3</sub> proceeded through the formation of intermediate lower oxides, prior to the production of the MO/Fe intermetallic alloys. Based on the intermediate phases that were identified and characterized at the early, intermediate, and final reduction degrees, chemical reaction equations were given to follow up the formation of the MoFe and MoFe<sub>3</sub> intermetallic alloys. The mechanism of the reduction reactions was predicted from the apparent activation energy values (*E<sub>a</sub>*) that were computed at the different reduction degrees. Moreover, mathematical formulations that were derived from the gas–solid reaction model were applied to confirm the reduction mechanisms, which were greatly dependent on the precursor composition and reduction temperature. However, it can be reported that nano-structured MoFe and MoFe<sub>3</sub> intermetallic alloys can be successfully fabricated via a gas–solid reaction technique at lower temperatures.

**Keywords:** iron; molybdenum; reduction; nanostructured materials; thermal powder technology; intermetallics; alloys and compounds; kinetics; mechanism; materials characterization; gas–solid reactions



**Citation:** El-Geassy, A.A.; Abdel Halim, K.S.; Alghamdi, A.S. A Novel Hydro-Thermal Synthesis of Nano-Structured Molybdenum-Iron Intermetallic Alloys at Relatively Low Temperatures. *Materials* **2023**, *16*, 2736. <https://doi.org/10.3390/ma16072736>

Academic Editor: Tomasz Czujko

Received: 27 February 2023

Revised: 23 March 2023

Accepted: 27 March 2023

Published: 29 March 2023



**Copyright:** © 2023 by the authors. Licensee MDPI, Basel, Switzerland. This article is an open access article distributed under the terms and conditions of the Creative Commons Attribution (CC BY) license (<https://creativecommons.org/licenses/by/4.0/>).

## 1. Introduction

Recently, the fabrication of metallic alloy materials has been considered to be an important issue for both scientific and industrial applications [1–5]. A gas–solid reaction technique

is considered to be a promising process and an environmentally friendly approach for the manufacturing of binary and tertiary metal alloys, as well as for the production of nano-structured intermetallics [6–11]. This technique is also widely applied to the production of metals from metal oxides and their ores [12,13]. The produced alloys have enough active centers to achieve good chemical bonding between the dispersed material and the matrix, and are widely applied within many engineering industries [14]. The composition and the morphology of the produced intermetallics can be controlled by adjusting the reaction parameters, such as the molar ratio of the reactants, the particle size, the reaction temperature, and the gas composition [15–17]. The produced tailor-made alloys can be further heat treated to improve their mechanical properties, prior to the manufacturing of micro-structured tools [18,19]. However, great attention has recently been paid to the use of these intermetallic alloys in semiconductors, photo-voltaic cells, special ceramics, and other chemical industries [20,21]. Intermetallic alloys have unique properties, particularly at high temperatures; hence, they can be developed as bases in the manufacturing of advanced materials that have different applications within the energy sector (power generation), transportation sector (automobile and aircraft production), and other engineering industries [22].

The pre-determined compositions of certain alloys can be produced from precursors that contain different molar ratios of intermetallics, via chemical co-precipitation, or sol-gel, thermal, and/or mechanical routes [23,24]. The co-precipitation technique is one of the most promising processes, due to its low cost, suitability for mass production, and production of high-purity alloys. About 80% of commercial molybdenum is used in metallurgical industries (35% in structural steel, 25% stainless steel, 9% in tools and high-speed steels, 6% in cast iron, and 5% in superalloys) [25]. Molybdenum is also used in the production of steel alloys, due to its high corrosion resistance and weldability, which increase the lattice strain and consequently increase the energy that is required to dissolve the iron atoms from the surface. On the other hand, molybdenum-based alloys that do not contain iron have limited applications. Morales [26] studied the production of an Fe<sub>2</sub>Mo alloy from a reduction of Fe<sub>2</sub>MoO<sub>4</sub> with H<sub>2</sub> gas in a fluidized bed reactor. FeMo intermetallics with different Fe/Mo molar ratios were synthesized from the reduction of the FeO-Fe<sub>2</sub>MoO<sub>4</sub>-MoO<sub>2</sub> mixtures with H<sub>2</sub>, at 600–750 °C. It was reported that the gas–solid reaction route, in combination with a powder technique, is a promising process towards the production of novel metallic alloys, such as the Fe<sub>2</sub>Mo intermetallic with micro- and nanocrystalline grains. In general, binary and tertiary ferrous and non-ferrous alloys can be produced from oxide mixtures via different techniques, such as mechanical alloying and/or electrodeposition techniques [27,28].

Nowadays, the gas–solid reduction technique is widely applied in ironmaking processes, in order to produce directly reduced iron (DRI) or so-called sponge iron for special steel production [29–33]. In this process, iron oxide (Fe<sub>2</sub>O<sub>3</sub>) is directly reduced with H<sub>2</sub> and/or CO to metallic iron, via intermediate reaction products (magnetite and/or wüstite) at relatively low temperatures.

The present study aims at a synthesis of the MoFe and MoFe<sub>3</sub> intermetallic alloys from the isothermal reduction of precursors that contain different molar ratios, with H<sub>2</sub> at relatively low temperatures. The reduction reaction mechanisms of the precursors were elucidated from the correlation between the apparent activation energy values (E<sub>a</sub>) and the application of the gas–solid heterogeneous mathematical formulations, which were derived from the gas–solid reaction model.

## 2. Materials and Experimental Procedure

### 2.1. Materials and Characterizations

Ammonium heptamolybdate tetrahydrate (AHM), with the chemical formula [(NH<sub>4</sub>)<sub>6</sub>Mo<sub>7</sub>O<sub>24</sub>·4H<sub>2</sub>O], and ferrous oxalate dihydrate (FeC<sub>2</sub>O<sub>4</sub>·2H<sub>2</sub>O) (Aldrich, Munich, Germany, >99.5% purity) were used for the preparation of two precursors containing 72/28% and 30/70% Mo/Fe molar ratios, named as precursor A and precursor B,

respectively. The pre-determined weights of the AHM and ferrous oxalate were dissolved in hot, bi-distilled water. The aqueous mixture was heated up to 70 °C with continuous stirring until it reached complete dryness. The different phases in the dry precipitate were identified by XRD (XRD, PAN Analytical Empyrean, Eindhoven, The Netherlands, 40 kV, 40 mA, Cu target, 1.543 Å). A TG-DSC simultaneous thermal analysis (STA 504 BÄHR Thermo-analyse, GmbH, Hüllhorst, Germany) was used to follow up the thermal behavior of the precursors during heating, in an Argon atmosphere of up to 700 °C. In this technique, the sample and inert sample (Al<sub>2</sub>O<sub>3</sub>) were subjected to a defined temperature program (isothermal or dynamic), and the changes in the mass and the heat turnover from the physical conversion and chemical reaction were recorded at the given times. A reflected light microscope (RLM, Axio-scope A1, Carl-Zeis Microscopy GmbH, Munich, Germany) and scanning electron microscope (SEM, JEOL-JSM-5410, Japan), coupled with electron dispersion spectroscopy (EDS, INCA Penta Fe Tx3, Oxford, UK), were used to examine the grain structure and morphology. The Mo, Fe, and oxygen elements were analyzed with EDS. A high-pressure mercury intrusion pore sizer of up to 30,000 psi (Micromeritics Instrument Corporation 9320, USA) was also applied for measuring the pore area, pore diameter, bulk density, apparent density, and total porosity in the roasted compacts.

## 2.2. Reduction Procedure

Uniform shape and size compacts from precursors A and B were formed from the pressing of about 2.0 g of a powder sample in a stainless mold, using a hydraulic press. The produced compacts (d = 4 mm, h = 6 mm) were kept dry in a desiccator. The reduction experiments were carried out isothermally at 600–850 °C in purified H<sub>2</sub> (NETCO, Cairo, Egypt, purity ≥ 99.9%), using a microbalance with a precision of ±0.1 µg (Mettler-Toledo XPR). The O<sub>2</sub> weight loss that resulted from the reduction reactions was continuously recorded as a function of time. The reduction and gas purification systems were given elsewhere [34]. The preliminary reduction tests indicated that 30 mL/min of the H<sub>2</sub> gas flow was sufficient to overcome the gas boundary layer effect around the sample. For a given experiment, the tube furnace was heated up to the pre-determined temperature in a continuous flow of purified Ar gas, then kept constant for 10 min. The dry compact, placed inside a platinum perforated basket, was hung from the balance arm with a platinum wire chain. The sample was slowly inserted into the furnace, continued to reach the hot zone, and was left for a while, in order to reach the pre-determined temperature. Under these conditions, the Ar gas was switched off and the H<sub>2</sub> gas (30 mL/min) was introduced into the reaction tube. The reduction reactions were started and continued until the sample reached a constant weight, showing that no more weight could be recorded. The reduced sample was cooled down to room temperature in a continuous flow of purified Ar gas until room temperature, then dropped in acetone to prevent re-oxidation reactions. The extent of the reduction ( $R_t$ ) that represents the reduction degree at a given time ( $t$ ) can be calculated from Equation (1), as the following:

$$R_t (\%) = (W_o - W_t) / W_o \times 100 \quad (1)$$

where  $W_o$  = the original weight of the sample, and  $W_t$  = the weight at a given time ( $t$ ).

For the partially reduced samples, the weight of the oxygen content ( $W_x$ ) at a given reduction extent ( $R_x$ ) was first calculated, the compact was subjected to the reduction experiment, and the O<sub>2</sub> weight loss was recorded until it reached the pre-calculated weight loss. Under these conditions, the furnace was switched off and the H<sub>2</sub> gas was replaced by Ar, and the sample was left to cool down to room temperature, then quickly dropped in acetone. The partially and/or completely reduced samples were analyzed and examined by XRD, (RLM), and SEM-EDS.

### 3. Results and Discussion

#### 3.1. Characterization of Materials

The dry powder precipitates from precursors A and B were thermally roasted in an air atmosphere of up to 700 °C using a TG-DSC analyzer, and their thermal behavior are given in Figure 1a,b, respectively. From the TG profile, the measured weight losses were 32.5% and 55.5%, which resulted from the thermal decomposition of the AHM and ferrous oxalate mixtures [35–37]. The thermal decomposition of the pure AHM was studied by H. Cavus et al., and they found that it decomposed to ammonium tetra molybdate (ATM)  $[(\text{NH}_4)_2\text{Mo}_4\text{O}_{13}]$  at 503 K, prior to the formation of  $\text{MoO}_3$  [35]. However, in the present study, different molar ratios of AHM and ferrous oxalate were co-precipitated to produce the precursors, and accordingly, the measured weight loss from the thermal analysis of precursors A and B was dependent on the molar ratio of each component in the precursors. The DSC profiles showed the presence of endothermic peaks at 97.8, 196.9, and 392.5–400 °C, which resulted from the removal of the moisture content, the decomposition of AHM to  $\text{MoO}_3$ , and the decomposition of ferrous oxalate to  $\text{Fe}_2\text{O}_3$ , respectively. The higher weight loss that was recorded in precursor B in comparison to precursor A resulted from the presence of an excess molar ratio of ferrous oxalate, which was greater than the stoichiometric ratio that produces the iron molybdate. The detection of exo- and endo-thermal peaks in the DSC analysis of both the precursors confirms the presence of more than one thermal decomposition reaction step, as discussed herein after [29].

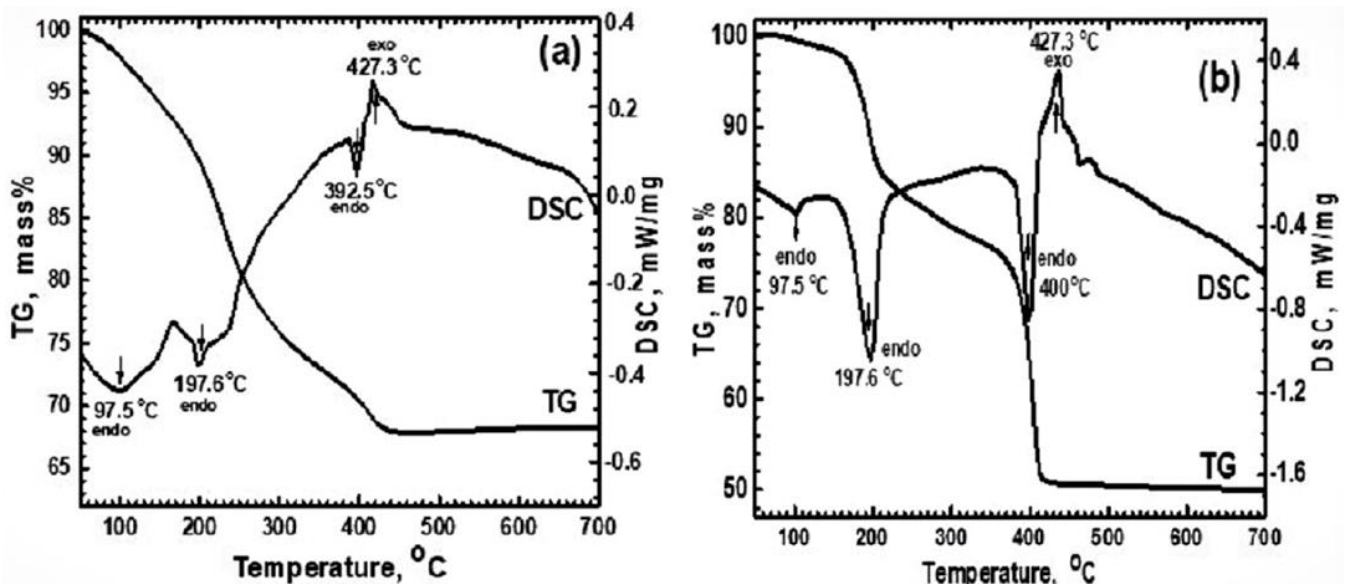
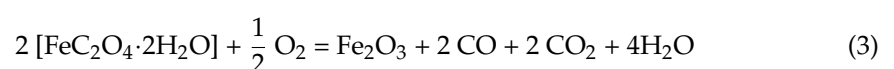
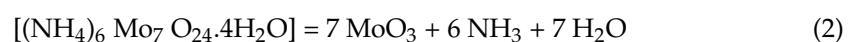
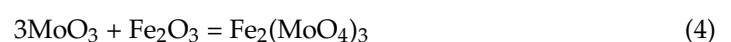


Figure 1. TG-DSC analysis of precursors thermally heated up to 700 °C in Ar gas atmosphere; (a) precursor A; and (b) precursor B.

The thermal decomposition reactions of the AHM and ferrous oxalate are given in Equations (2) and (3), respectively, as follows.



The exothermic peak that was measured at 427.3–430 °C (Figure 1a) resulted from the solid-state reaction between  $\text{MoO}_3$  (Equation (2)) and  $\text{Fe}_2\text{O}_3$  (Equation (3)) to produce the iron molybdate  $\text{Fe}_2(\text{MoO}_4)_3$ , as given in Equation (4):



The reaction products that were obtained from the thermal treatment of up to 700 °C of precursors A and B, given in Equations (2)–(4), were subjected to an XRD phase analysis that confirmed the above findings. From Figure 1, it can be observed that no more weight loss was recorded at >430 °C, which indicated that the dissociation and solid-state reactions were completed. Accordingly, green compacts were made from precursors A and B and thermally heated at 500 °C for 3 h in an Ar gas atmosphere, and the products were characterized. Table 1 shows the chemical compositions, phases identified, molar ratios, total porosity, and apparent density that were measured in the roasted precursors. The micro- and macro-structures were microscopically examined, and the phases were elementally analyzed by EDS.

**Table 1.** Characteristics and phases identified in precursors roasted at 500 °C for 3 h.

Precursor	Composition		Phases Identified	Molar Ratio (%)	Total Porosity (%)	Apparent Density (g/mL)
	Mo %	Fe %				
(A)	72	28	Fe <sub>2</sub> (MoO <sub>4</sub> ) <sub>3</sub>	100	59.87	6.43
(B)	30	70	Fe <sub>2</sub> (MoO <sub>4</sub> ) <sub>3</sub> α-Fe <sub>2</sub> O <sub>3</sub>	46.68 53.32	48.39	5.35

It was found that iron molybdate [Fe<sub>2</sub>(MoO<sub>4</sub>)<sub>3</sub>] was the only phase that was identified in precursor A, while in precursor B, α-Fe<sub>2</sub>O<sub>3</sub> and [Fe<sub>2</sub>(MoO<sub>4</sub>)<sub>3</sub>] were identified. The presence of excess Fe<sub>2</sub>O<sub>3</sub> in precursor B hindered the grain growth of the iron molybdate, which, in turn, affected the total porosity and apparent density.

Figure 2 shows the RLM photomicrographs and the SEM images for the roasted precursors A and B. The photomicrograph that is given in Figure 2a shows the formation of different grain sizes of the iron molybdate. The larger grains were composed of large numbers of smaller grains, with different shape and sizes that were embedded together in a matrix, which were sintered forming clusters. These grains coalesced with each other, forming aggregates that left large pores. The SEM image that is given in Figure 2b shows the formation of the large sizes of grains, which were bonded together through the neck at the points of collision, forming aggregates. On the other hand, the photomicrographs of precursor B, which are given in Figure 2c, show the presence of relatively large numbers of smaller-size grains, compared to those in precursor A. The smaller grains were mainly composed of hematite, while iron molybdate was in the larger grains. The SEM image for precursor B, which is given in Figure 2d, shows the formation of rounded grains of iron molybdate and hematite, which have an average size of 194 nm. The higher porosity that was measured in precursor A than that in B was due to the presence of larger pores between the agglomerated grains.

### 3.2. Reduction Behavior

#### 3.2.1. Influence of Reduction Temperature

The compacts from precursors A and B were isothermally reduced at 600–850 °C in the H<sub>2</sub> gas. The reduction degree at a given time was calculated by applying Equation (1), taking into consideration the maximum O<sub>2</sub> weight loss that was measured from the reduction reactions represented 100%, since no more weight loss was recorded. Consequently, the relative reduction degrees (%) at a given time were calculated relative to the maximum reducible O<sub>2</sub> content that was measured in the precursors. The reduction behavior of precursors A and B is shown in Figure 3a,b, respectively. It was found that the reduction at <600 °C was very slow and stopped before completion, depending on the precursor composition. At >850 °C, the reduced products swelled, showing an increase in volume of 175% and 140% for precursors A and B at 900 °C, respectively. For precursor A, composed of 100% iron molybdate, the rate of reduction increased with a rise in temperature and decreased with an increase in the reduction extents. It can be observed that the temperature had a relatively considerable influence on the reduction rate, showing a higher difference

up to 750 °C, above which, the difference in the rate was decreased. For a given reduction path at <700 °C, the rate during the early stages was gradually decreased with time, up to certain extent, above which, there was a considerable decrease in the rate until the end of the reduction process. During the early stages, the rate started to decrease from a 30% extent at 750 °C to about 24% at 650 °C, and then to 14% at 600 °C. During the later stages, the rate gradually decreased until the end of the reduction process, showing a slowing in the rate. At  $\geq 750$  °C, the reduction of the precursor was fast, up to a certain extent, after which, an abrupt decrease showed a slowing in the rate during the final stages, which decreased with a rise in the temperature. The presence of a slowing in the rate indicated that the reduction could not be continued by a gas–solid reaction, and most probably, the solid-state diffusion contributed to the reduction reactions.

For precursor B, which was composed of 53.32%  $\alpha$ -Fe<sub>2</sub>O<sub>3</sub> and 46.68% Fe<sub>2</sub>(MoO<sub>4</sub>)<sub>3</sub>, the typical reduction curves are shown in Figure 3b. The same behavior can be observed, where the rate of the reduction was increased, increasing the reduction temperature. During the early stages, the reduction path at 600 °C was significantly lower than that at 650 °C, above which, the reduction paths were closer to each other up to 850 °C. During the intermediate stages, the reduction rate was greatly decreased until the end of the reduction. Unlike in precursor A, the reduction at  $\leq 650$  °C was completed, and the rate gradually decreased until the end of the reduction reactions.

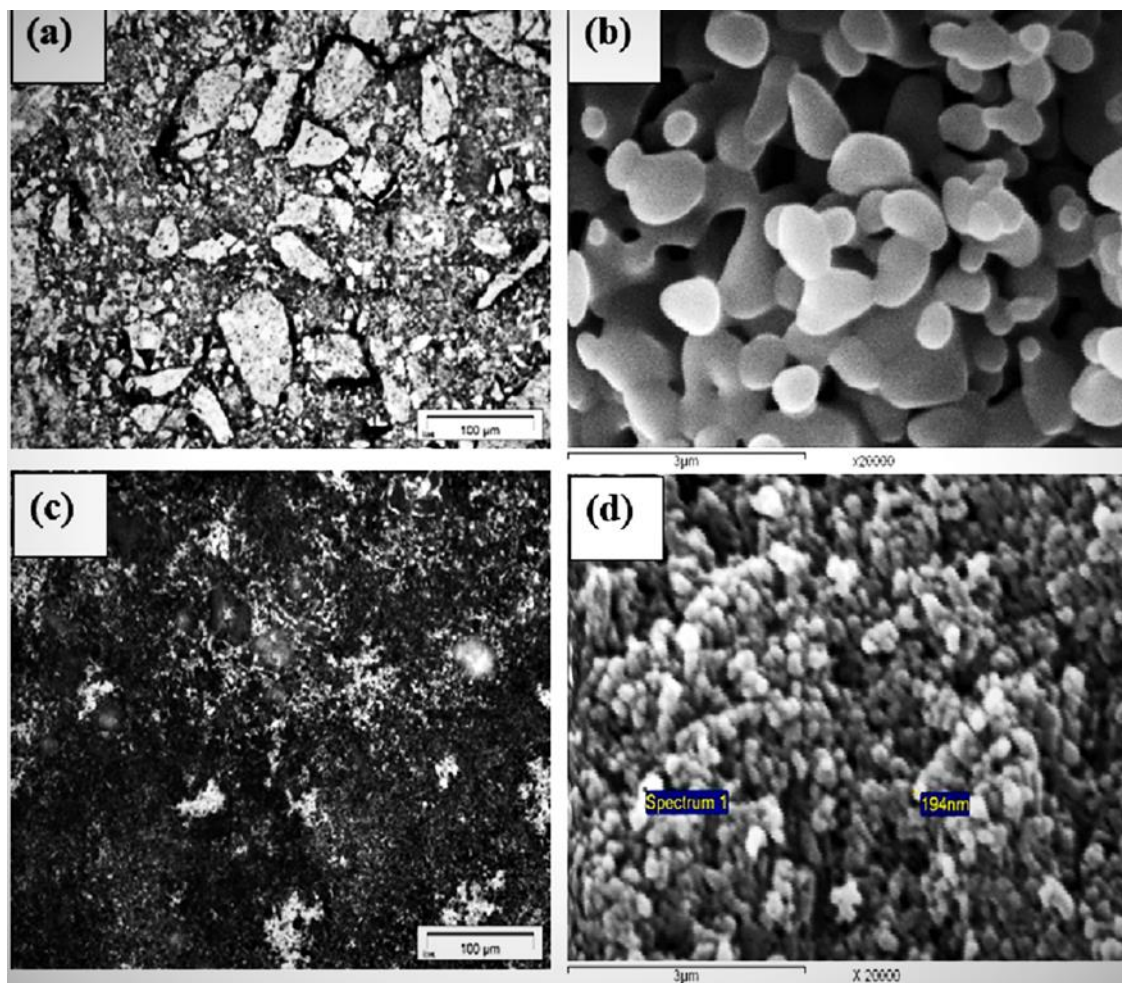


**Figure 2.** RLM photomicrographs and SEM image for precursor compacts thermally heated up to 500 °C in Ar gas atmosphere; (a,b) for precursor A; and (c,d) for precursor B.

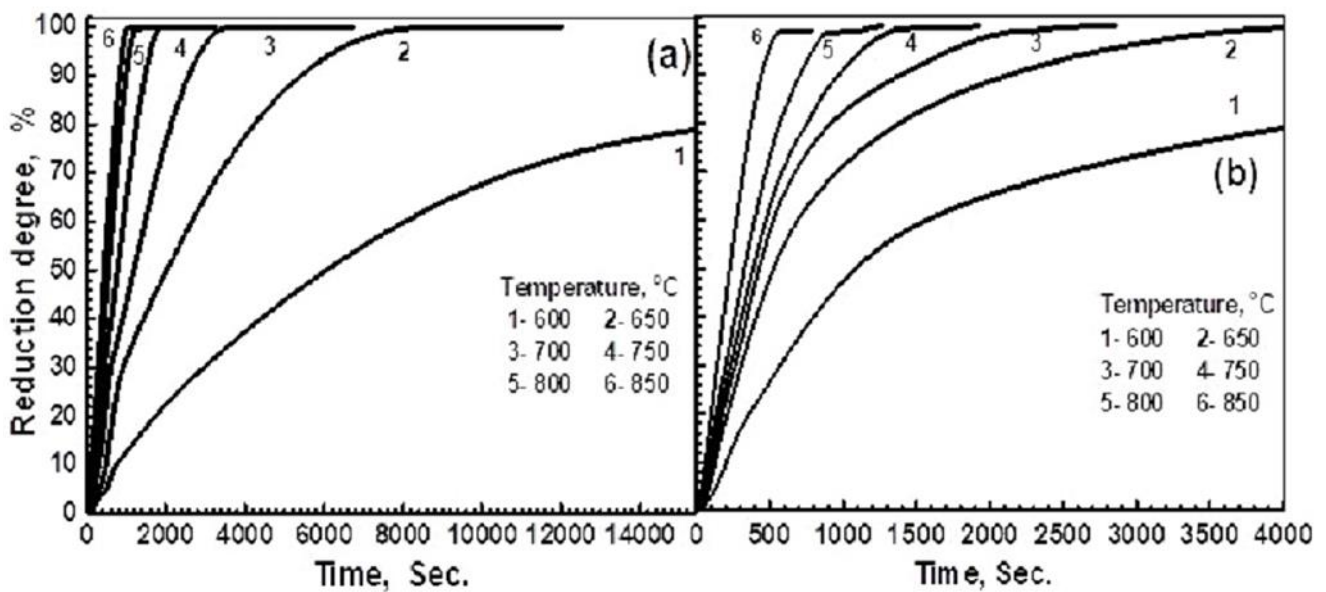


**Figure 3.** Isothermal reduction behavior of precursors with H<sub>2</sub> at 600–850 °C; (a) precursor A; and (b) precursor B.

In order to follow up the reduction reactions of the precursors and the formation of the intermediate reaction products, precursors A and B were partially reduced up to 20, 60, and 85% extents. The partially and completely reduced samples were examined by XRD, RLM, and SEM-EDAX. Figure 4a,b show the typical XRD patterns of the partially and completely reduced samples from precursors A and B at 750 °C, respectively. Figure 4a shows that Fe<sub>2</sub>(MoO<sub>4</sub>)<sub>3</sub> was stepwisely reduced to lower oxides, prior to the formation of the MoFe intermetallic and Mo. Figure 4b shows that, in precursor B, besides the formation of lower oxides from the reduction reactions of Fe<sub>2</sub>(MoO<sub>4</sub>)<sub>3</sub>, Fe<sub>2</sub>O<sub>3</sub> was also stepwisely reduced to Fe<sub>3</sub>O<sub>4</sub> and/or wüstite (FeO), and finally to α-Fe. In this precursor, the final reaction products were MoFe, MoFe<sub>3</sub> intermetallics, and α-Fe.

The different phases that were identified from the reduction reactions of precursors A and B at the 20, 60, 85, and 100% extents are given in Table 2.

From Table 2, it can be seen that Fe<sub>2</sub>(MoO<sub>4</sub>)<sub>3</sub> was stepwisely reduced to Fe<sub>2</sub>Mo<sub>3</sub>O<sub>8</sub>, FeMoO<sub>4</sub>, and MoO<sub>2</sub> phases before the final production of the MoFe intermetallics and metallic Mo in precursor A. In precursor B, the stepwise reduction of Fe<sub>2</sub>(MoO<sub>4</sub>)<sub>3</sub> and Fe<sub>2</sub>O<sub>3</sub> led to the synthesis of the FeMo and Fe<sub>3</sub>Mo intermetallics and metallic Fe in the final reaction product.

The SEM images for precursors A and B, partially and completely reduced at 750 °C (up to 20%, 60%, 85%, and 100% extents), are given in Figures 5 and 6, respectively. EDS was applied to analyze the Mo, Fe, and oxygen in the different phases. Figure 5a shows the structure of the 20% reduced compact, in which Fe<sub>2</sub>(MoO<sub>4</sub>)<sub>3</sub> is reduced to [Fe<sub>2</sub>Mo<sub>3</sub>O<sub>8</sub>] in a needle shape and has a parallel orientation alongside the presence of the irregular grains of MoO<sub>2</sub>. With an increase in the reduction extent of up to 60% (Figure 5b), FeMoO<sub>4</sub> is further reduced to MoO<sub>2</sub> and FeMoO<sub>4</sub>, while Fe<sub>2</sub>Mo<sub>3</sub>O<sub>8</sub> is still also identified. In the 85% reduced sample (Figure 5c), Fe<sub>2</sub>Mo<sub>3</sub>O<sub>8</sub>, MoFe, and Mo are present. In the completely reduced precursor (Figure 5d), MoFe intermetallics are the predominant phase that is identified in the form of the whiskers together, with small grains of Mo metal. Unlike the grain structure that was developed in precursor A, the grain structure that was formed in precursor B differs, due the presence of an excess molar ratio of iron oxides. The grain structure of the 20% reduced sample, which is given in Figure 6a, shows the presence of Fe<sub>2</sub>O<sub>3</sub> and Fe<sub>3</sub>O<sub>4</sub> in smaller grain sizes, alongside the lower oxides of the iron molybdate in different grain structures. The needles structure of Fe<sub>2</sub>Mo<sub>3</sub>O<sub>8</sub> is still present. The FeMoO<sub>4</sub> phase is present in dense grains, while MoO<sub>2</sub> is formed in the matrix as smaller grains. The structure that developed in the 60% reduced sample (Figure 6b) shows the presence of magnetite and



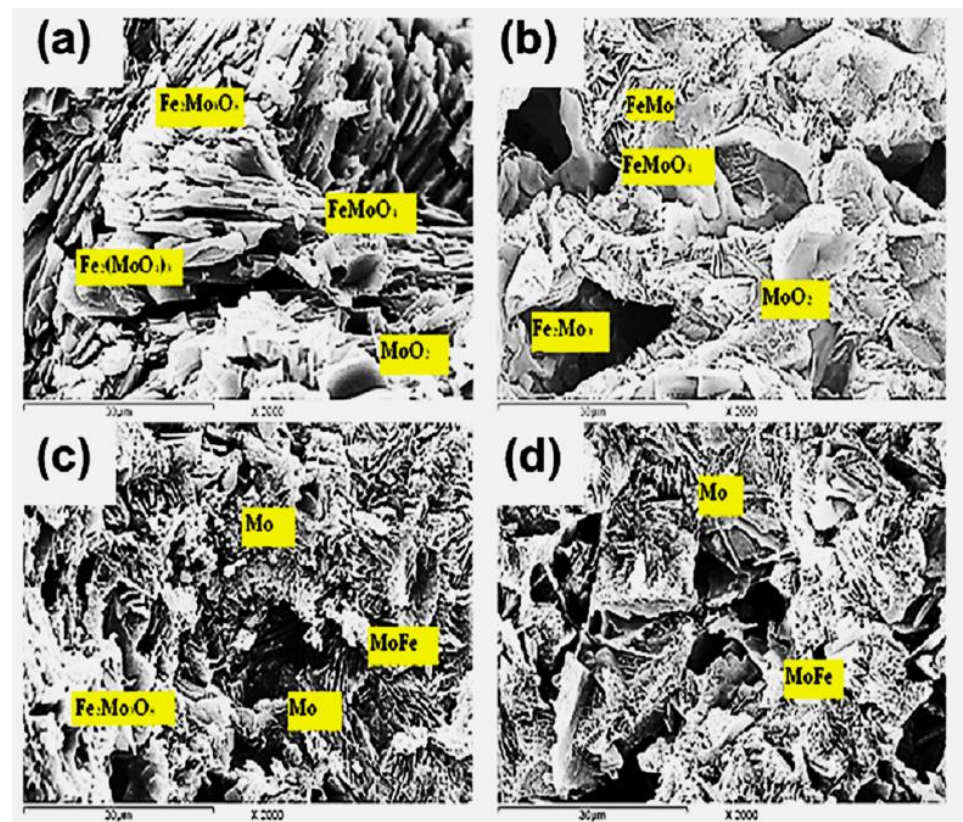


**Figure 5.** SEM images analysis for precursors (A) reduced at 750 °C with H<sub>2</sub> up to (a) 20%; (b) 60%; (c) 85%; and (d) 100% degrees.

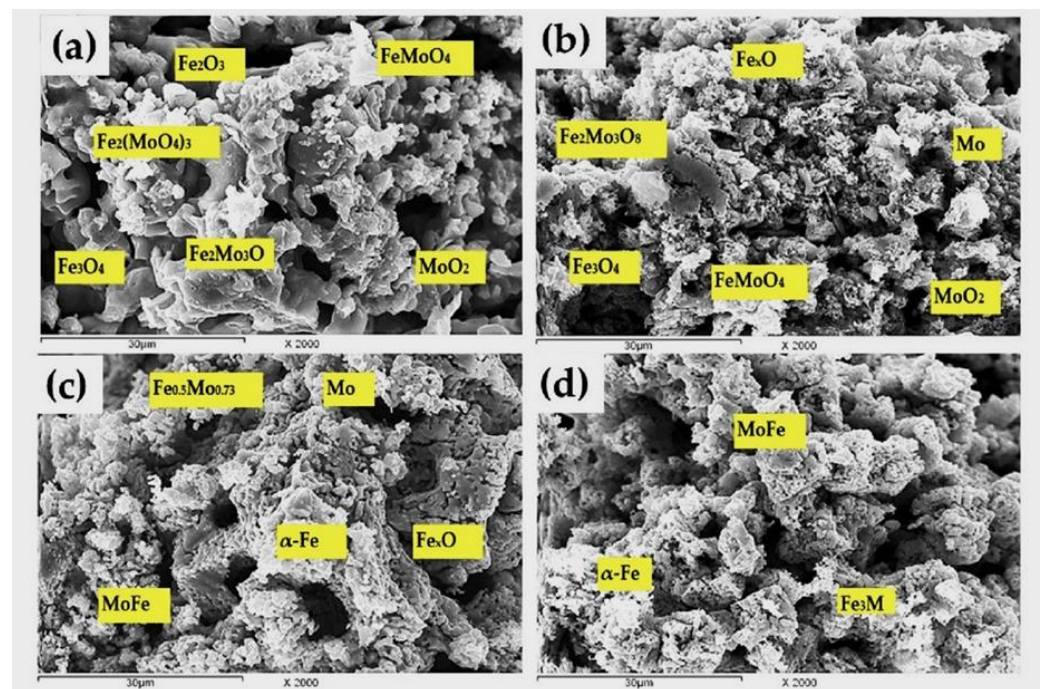


**Figure 6.** SEM images analysis for precursors (B) reduced at 750 °C with H<sub>2</sub> up to (a) 20%; (b) 60%; (c) 85%; and (d) 100% degrees.

### 3.2.2. Influence of Precursor Composition

The isothermal reduction behavior of precursors A and B with  $H_2$ , at 650, 700, 750, and 800 °C, are given in Figure 7a–d, respectively. It can be seen that the rate of reduction for precursor B is higher than that for precursor A, at all temperatures, and proceeds smoothly, in which the rate gradually decreases with an increase in the reduction extent until the end of reduction process. On the other hand, the reduction of precursor A shows that the rate of reduction is lower during the early stages, depending on the reduction temperature, then increases up to about a 20% extent, above which, the rate gradually decreases to about a 95% extent. During the later stages, a slowing in the rate of reduction is clearly identified, with special emphasis on precursor A rather than B. This is mainly due to the presence of excess  $Fe_2O_3$  than the stoichiometric ratio which is required to produce iron molybdate.

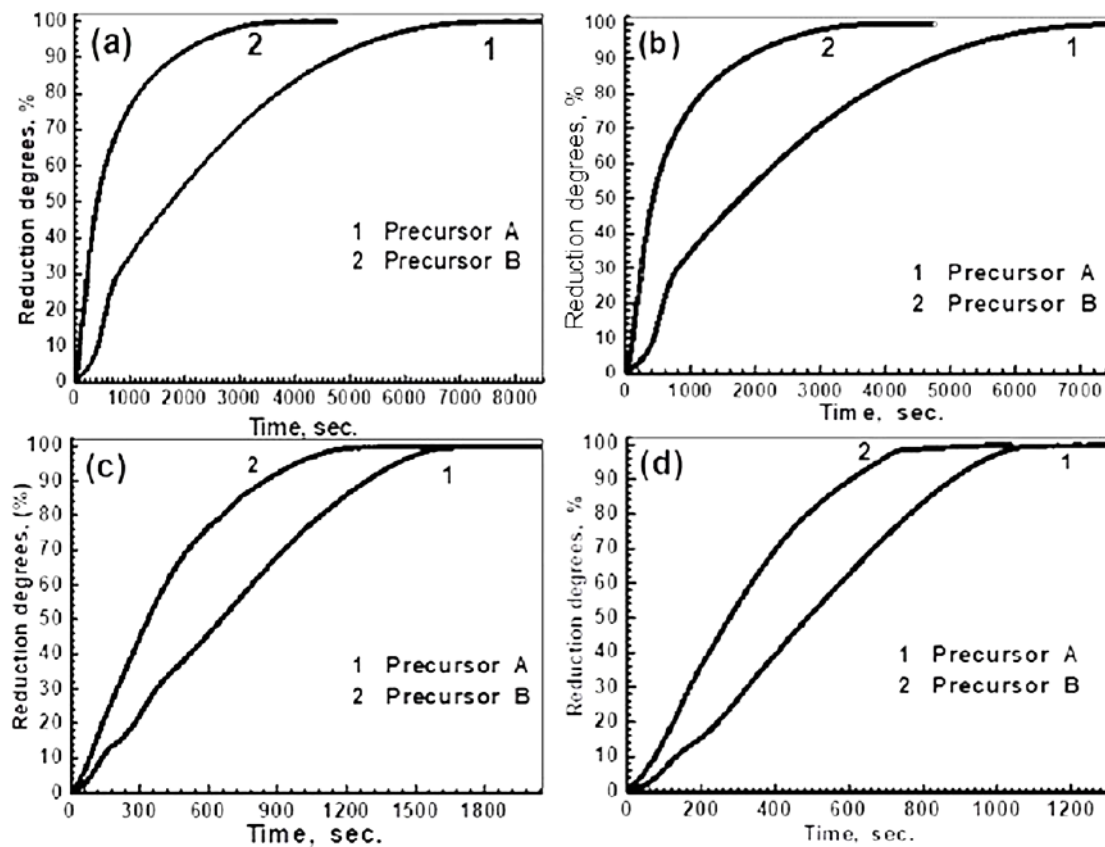
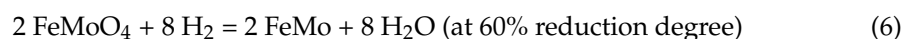


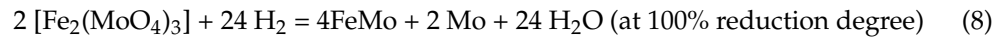
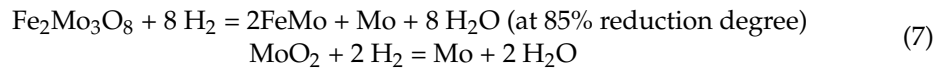
**Figure 7.** Influence of precursor composition on the isothermal reduction behavior with  $H_2$  at (a) 650 °C; (b) 700 °C; (c) 750 °C; and (d) 800 °C.

### 3.3. Chemistry of Intermetallics Formation

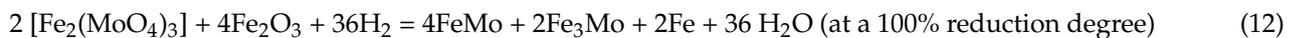
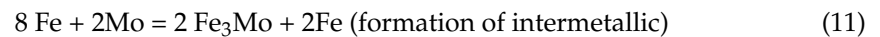
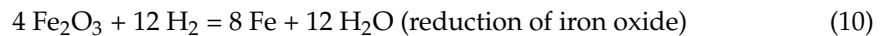
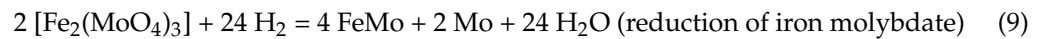
The reduction reactions of the  $Fe_2(MoO_4)_3$  and  $Fe_2O_3$  phases in the precursors with  $H_2$  were found to proceed through the formation of intermediate reaction products, prior to the synthesis of the MoFe and  $MoFe_3$  intermetallic alloys, as previously given in Table 2. Based on the intermediate reaction phases that were identified at the different reduction extents, the chemical reaction equations that describe the reduction reactions of the precursors can be formulated as follows:

1. The chemical reaction equations of precursor A,  $[100\% Fe_2(MoO_4)_3]$





2. The chemical reaction equations of precursor (B), [46.68%  $\text{Fe}_3(\text{MoO}_4)_3$  + 53.32%  $\text{Fe}_2\text{O}_3$ ];



From the chemical reaction equations, depending on the precursor composition, it can be reported that the MoFe intermetallics and Mo are obtained from the reduction of precursor A, while MoFe, the  $\text{MoFe}_3$  intermetallics, and Fe are produced from the reduction of precursor B. Such a conclusion agrees with the XRD phase analysis that is given in Table 2 and the microstructure changes that are given in Figures 5 and 6.

### 3.4. Reduction Kinetics and Mechanisms

Thermodynamic analysis is an important issue in the synthesis and characterization of intermetallic alloys from their original material, via gas–solid reaction processes. The mechanism of the reduction reaction can be predicted from both the apparent activation energy ( $E_a$ ) values, which are calculated from Arrhenius plots, and also from the application of the mathematical formulations that are derived from the gas–solid model.

The apparent activation energy values ( $E_a$ ) can be calculated from the application of the Arrhenius equation [38];

$$K_r = K_0 \cdot e^{-E_a/RT} \quad (13)$$

Where  $K_r$  is the reduction rate constant,  $K_0$  is the frequency factor,  $R$  is the gas constant, and  $T$  is the absolute temperature. Figure 8a,b represent the Arrhenius plots, in which the ( $\log dr/dt$ ) values that were calculated at the different reduction extents are plotted against the corresponding ( $1/T$ ) for precursors (A) and (B), respectively. The  $E_a$  values that were computed during the early, intermediate, and later stages of the reduction, together with the proposed reduction mechanism, are given in Table 3.

The calculated  $E_a$  values can be used to predict the reduction mechanism. For precursor A, the reduction during the early stages (up to 10%) is controlled by the combined effects of the gas diffusion and interfacial chemical reaction mechanism. With an increase in the reduction extent, the contribution of the interfacial chemical reaction increases until it becomes the rate-controlling mechanism, up to about an 85% extent, which is dependent on the applied temperature. During the later stages ( $\geq 90\%$  extent), the reduction of precursor A at  $\geq 750$  °C is still controlled by the interfacial chemical reaction. At  $\leq 700$  °C, the reduction reaction is controlled by the solid-state diffusion mechanism, resulting in the slowing of the rate until the end of the reduction reaction.

On the other hand, the reduction of precursor B is controlled by the gaseous diffusion mechanism up to a 10% extent, after which, the contribution of the interfacial chemical reaction increases until it becomes the rate-determining mechanism, up to about a 90% extent. During the later stages, the interfacial chemical reaction is the rate-controlling mechanism at  $\geq 750$  °C. At  $\leq 700$  °C, the solid-state diffusion seems to be the rate-controlling mechanism until the end of the reduction process.

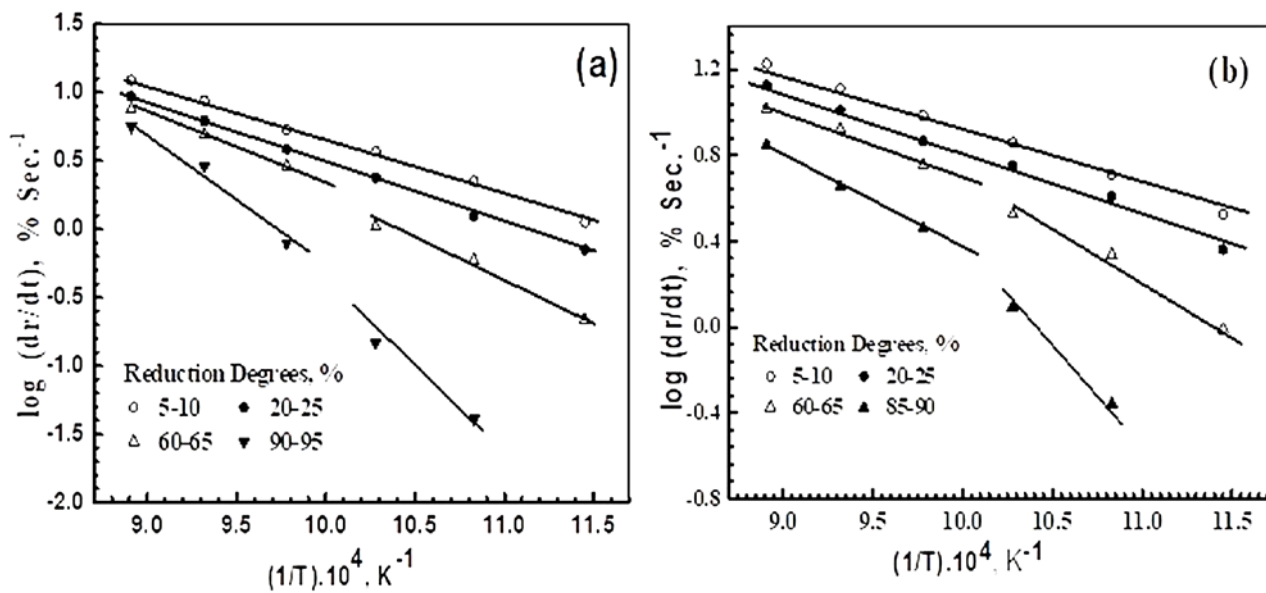


**Figure 8.** Arrhenius plots for the reduction of precursors with H<sub>2</sub> at 600–850 °C: (a) precursor A; and (b) precursor B.

**Table 3.**  $E_a$  values computed for the reduction of precursors at 600–850 °C and the proposed corresponding reaction mechanism.

Reduction Degree, %	$E_a$ , kJ mole <sup>-1</sup>		Rate Controlling Mechanism according to the Reference Values of Activation Energy, [29]	
	Precursor (A)	Precursor (B)	$E_a$ , (kJ mole <sup>-1</sup> )	Controlling mechanism
5–10%	25.63	15.87	$E_a$ , (kJ mole <sup>-1</sup> )	Controlling mechanism
20–25%	48.09	32.31	8–16	Gas diffusion
60–70%	65.23	48.98	29–42	Gas diffusion and interfacial chemical reaction
90–95%	at $\geq 750$ °C	85.32	60–70	Interfacial chemical reaction
	at $\leq 700$ °C	125.79	94.85	>90

In another way to confirm our findings regarding the mechanisms of reduction, the gas–solid reaction model [11,32,33,39] was performed. The simplified formulations of the gas diffusion, interfacial chemical reaction, and mixed control mechanism that were derived from the gas–solid reaction model are:

$$P_{Fg}(X) = [X + (1 - X) \ln(1 - X)] = K_1 t \text{ (gaseous diffusion control)} \quad (14)$$

$$t^* = [1 - (1 - X)^{1/Fg}] = K_2 t \text{ (interfacial chemical reaction control)} \quad (15)$$

$$t^* = [X + (1 - X) \ln(1 - X)] + [1 - (1 - X)^{1/Fg}] = K_3 t \text{ (mixed control reaction)} \quad (16)$$

where  $K_1$ ,  $K_2$ , and  $K_3$  are constants (sec<sup>-1</sup>);  $X$  is the fractional reduction degree ( $Rt/100$ ) calculated at a given time ( $t$ ), as defined in Equation (1);  $t^*$  is the dimensionless time; and  $Fg$  is the shape factor (1 and 2 for grains and compacts, respectively).

The mathematical formulations that are given in Equations (14)–(16) were tested against the experimental reduction reaction results of precursors A and B. For precursor A, the testing of the three mathematical equations resulted in only straight lines upon applying Equation (15), as shown in Figure 9a. These straight lines are valid from 15%, up to certain extent, depending on the applied temperature. At  $\geq 750$  °C, the straight lines are valid up until the later stages of the reduction, which indicates that the reduction reaction

is controlled by the interfacial chemical reactions mechanism. At  $<700\text{ }^{\circ}\text{C}$ , the straight lines are deviated at the different reduction extents (Figure 9a). This indicates that the reduction is controlled by the interfacial chemical reaction mechanism, up to certain extent, beyond which, the solid-state diffusion contributes with the interfacial chemical reaction and becomes the rate-determining mechanism.

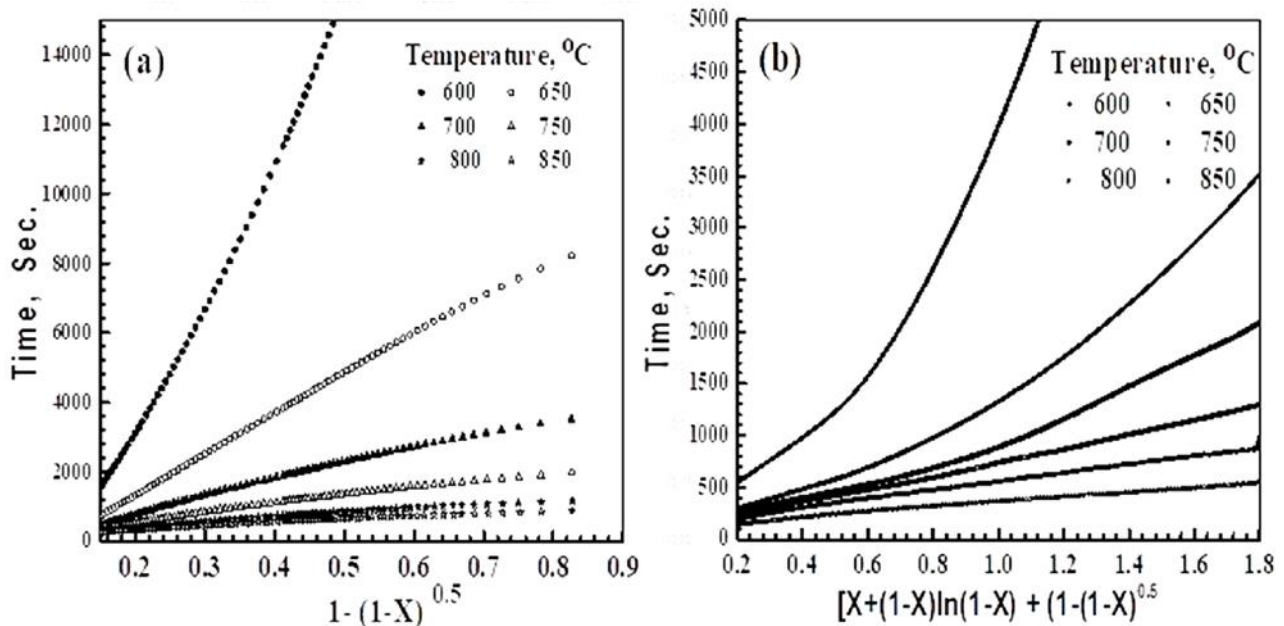


**Figure 9.** Application of mathematical equations for the reduction of precursors at 600–850 °C in  $\text{H}_2$ : (a) precursor A; and (b) precursor B.

Figure 9b shows the application of the mixed control reaction formulation (Equation (16)) against the reduction results of precursor B. The presence of two sets of lines can be observed, in which straight lines are obtained at  $\geq 750\text{ }^{\circ}\text{C}$ , beyond which, the straight lines are deviated at different extents, depending on the applied temperatures. This indicates that the reduction is controlled by the combined effects of gas diffusion and the interfacial chemical reaction mechanism (mixed control mechanism). At higher temperatures, the contribution of the interfacial chemical reaction in the mixed mechanism increased with an increase in the reduction extents, and decreased with a rise in temperature. At  $\leq 700\text{ }^{\circ}\text{C}$ , the reduction is controlled by the mixed reaction mechanism, up to a certain extent, and then by the interfacial chemical reaction mechanism until the end of the reduction process.

#### 4. Conclusions

The gas–solid reaction technique is successfully applied to produce nano-structured MoFe and/or MoFe<sub>3</sub> intermetallics from the reduction of precursors that contained 72/28 and 30/70% molar ratios, named as precursors A and B, respectively. Both precursors were prepared from the co-precipitation of AHM and ferrous oxalate. Their roasted compacts were isothermally reduced in  $\text{H}_2$  at 600–850 °C. The reduction of precursor A showed that  $[\text{Fe}_2(\text{MoO}_4)_3]$  was reduced to lower intermediate oxides, prior to the production of the MoFe intermetallic and Mo. On the other hand, MoFe and MoFe<sub>3</sub> intermetallics, together with metallic Fe, were obtained from the reduction reactions of precursor B. The rate of reduction of precursor B was much higher than that of precursor A, at all temperatures, due to the presence of an excess molar ratio of  $\text{Fe}_2\text{O}_3$ , which was greater than the stoichiometric molar ratio that produces  $[\text{Fe}_2(\text{MoO}_4)_3]$ . Depending on the intermediate reaction products, which were identified by XRD and examined by SEM-EDS, the chemical reaction equations that were given aimed at following up the synthesis of the intermetallic alloys (MoFe and MoFe<sub>3</sub>).

The mechanisms of the reduction reactions of precursors A and B during the early, intermediate, and later stages were elucidated from the correlations between the computed activation energy ( $E_a$ ) values and the applications of the mathematical formulations that were derived from the gas–solid reaction model. The reduction mechanism was greatly dependent on the precursor composition and reduction temperature. It was concluded that the reduction reaction mechanism of precursor A was controlled by the combined effect of a gas diffusion and an interfacial chemical reaction mechanism, up to about a 15% extent, above which, the reduction reaction was controlled by the interfacial chemical reaction, until about a 85% extent. With progress in the reduction process, the solid state-diffusion contributed, with the interfacial chemical reaction, as the rate-controlling mechanism. During the later stages, the contribution of the solid-state diffusion increased and it became the rate-controlling mechanism. The reduction of precursor B was controlled by gas diffusion during its early stages, followed by higher contribution of the interfacial chemical reaction until the later reduction stages. During the final stages, the solid-state diffusion slightly contributed with the interfacial chemical reaction.

From this study, it can be concluded that the gas–solid reaction technique can be successfully applied to produce nano-structured and nano-sized intermetallic alloys. A reduction with  $H_2$  gas is considered to be an environmentally friendly approach and can be extended to the synthesis of binary and tertiary metal alloys.

**Author Contributions:** Conceptualization, A.A.E.-G.; methodology, A.A.E.-G., A.S.A. and K.S.A.H.; software, A.A.E.-G. and K.S.A.H.; validation, A.A.E.-G., K.S.A.H. and A.S.A.; formal analysis, A.A.E.-G., K.S.A.H. and A.S.A.; investigation A.A.E.-G., K.S.A.H. and A.S.A.; resources, A.A.E.-G.; data curation, A.A.E.-G. and K.S.A.H.; writing—original draft preparation, A.A.E.-G., K.S.A.H. and A.S.A.; writing—review and editing, A.A.E.-G. and K.S.A.H.; visualization, A.A.E.-G., K.S.A.H. and A.S.A.; supervision, A.S.A.; project administration, K.S.A.H.; funding acquisition, A.S.A. All authors have read and agreed to the published version of the manuscript.

**Funding:** This research has been funded by Scientific Research Deanship at University of Ha'il—Saudi Arabia through project number RG-22 028.

**Institutional Review Board Statement:** Not applicable.

**Informed Consent Statement:** Not applicable.

**Data Availability Statement:** Not applicable.

**Conflicts of Interest:** The authors declare no conflict of interest.

## References

1. Biserova-Tahchieva, A.; Biezma-Moraleda, M.V.; Llorca-Isern, N.; Gonzalez-Lavin, J.; Linhardt, P. Additive Manufacturing Processes in Selected Corrosion Resistant Materials: A State of Knowledge Review. *Materials* **2023**, *16*, 1893. [[CrossRef](#)] [[PubMed](#)]
2. Bahgat, M.; Paek, M.K.; Pak, J.J. Hydrogen Reduction of  $Fe_2O_3/WO_3$  Mixture with Synthesis of Nanocrystalline Fe/W Composite. *Mater. Trans.* **2008**, *49*, 1480. [[CrossRef](#)]
3. Lakshmikanthan, A.; Angadi, S.; Malik, V.; Saxena, K.K.; Prakash, C.; Dixit, S.; Mohammed, K.A. Mechanical and Tribological Properties of Aluminum-Based Metal-Matrix Composites. *Materials* **2022**, *15*, 6111. [[CrossRef](#)] [[PubMed](#)]
4. Niinomi, M.; Nakai, M.; Hieda, J. Development of new metallic alloys for biomedical applications. *Acta Biomater.* **2012**, *8*, 3888–3903. [[CrossRef](#)] [[PubMed](#)]
5. Olekšáková, D.; Kollár, P.; Neslušan, M.; Jakubčín, M.; Füzér, J.; Bureš, R.; Fáberová, M. Impact of the Surface Irregularities of NiFeMo Compacted Powder Particles on Irreversible Magnetization Processes. *Materials* **2022**, *15*, 8937. [[CrossRef](#)]
6. Ahmed, H.M.; El-Geassy, A.A.; Seetheraman, S. Kinetic studies of hydrogen reduction of NiO- $WO_3$  precursors in fluidized bed reactor. *ISIJ Int.* **2011**, *51*, 1359–1367. [[CrossRef](#)]
7. Abdel Halim, K.S. Novel synthesis of porous Fe–Ni ferroalloy powder for energy applications. *Mater. Lett.* **2012**, *68*, 478. [[CrossRef](#)]
8. Nasr, M.I.; Omar, A.A.; Khedr, M.H.; EL Geassy, A.A. Effect of nickel oxide iron oxide reduction doping on the kinetics and mechanism of iron oxide reduction. *ISIJ Int.* **1995**, *35*, 1043–1049. [[CrossRef](#)]
9. Simić, L.; Stopić, S.; Friedrich, B.; Zadravec, M.; Jelen, Ž.; Bobovnik, R.; Anžel, I.; Rudolf, R. Synthesis of Complex Concentrated Nanoparticles by Ultrasonic Spray Pyrolysis and Lyophilisation. *Metals* **2022**, *12*, 1802. [[CrossRef](#)]

10. Abdel Halim, K.S.; Bram, M.; Buchkremer, H.P.; Bahgat, M. Synthesis of heavy tungsten alloy by thermal technique. *Ind. Eng. Chem. Res.* **2012**, *51*, 16354–16360. [CrossRef]
11. Al-Kelesh, H.; Abdel Halim, K.S.; Nasr, M.I. Synthesis of heavy tungsten alloys via powder reduction technique. *J. Mater. Res.* **2016**, *31*, 2977–2986. [CrossRef]
12. El-Geassy, A.A. Gaseous reduction of pure Fe<sub>2</sub>O<sub>3</sub> and MgO-doped Fe<sub>2</sub>O<sub>3</sub> compacts with carbon monoxide at 1173–1473 K. *J. Iron Steel Inst. Jpn. Int.* **1996**, *36*, 1328–1337. [CrossRef]
13. El-Geassy, A.A. Gaseous reduction of Fe<sub>2</sub>O<sub>3</sub> compacts at 600–1050 °C. *J. Mater. Sci.* **1986**, *21*, 3889–3900. [CrossRef]
14. Tremel, W.; Kleinke, H.; Derstroff, V.; Reisner, C. Transition metal chalcogenides: New views on an old topic. *J. Alloy. Compd.* **1995**, *219*, 73–82. [CrossRef]
15. King, P.L.; Fegley, B.; Seward, T. High Temperature Gas-Solid Reactions in Earth and Planetary Processes. *Rev. Mineral. Geochem.* **2018**, *84*, 4. [CrossRef]
16. Abdel Halim, K.S.; Ramadan, M.; Shawabkeh, A.; Abufara, A. Synthesis and characterization of metallic materials for membrane technology. *Beni-Suef Univ. J. Basic Appl. Sci.* **2013**, *2*, 72–79. [CrossRef]
17. Arun, R. Size-dependent fracture characteristics of intermetallic alloys. *Exp. Mech.* **2022**, *62*, 863–877. [CrossRef]
18. Metzger, F.; Rienzi, V.; Mascetti, C.; Nguyen, T.; Pimputkar, S. Properties of Titanium Zirconium Molybdenum Alloy after Exposure to Indium at Elevated Temperatures. *Materials* **2022**, *15*, 5270. [CrossRef]
19. Panel on Intermetallic Development. *Intermetallic Alloy Development: A Program Evaluation*; Panel on Intermetallic Development, National Research Council (U.S.) Publication NMAB-487-1; National Academy Press: Washington, DC, USA, 1997.
20. Song, C.; Wang, S.; Gui, Y.; Cheng, Z.; Ni, G. Microstructure and Tribological Properties of Mo–40Ni–13Si Multiphase Intermetallic Alloy. *Materials* **2016**, *9*, 986. [CrossRef]
21. Mendiratta, M.G.; Dimiduk, D.M.; Kim, Y.W.; Miracle, D.B. Recent progress on intermetallic alloys for advanced aerospace systems. *ISIJ Int.* **2008**, *31*, 1223–1234.
22. Gostishchev, V.V.; Astapov, I.A.; Khimukhin, S.N. Exothermic synthesis of cast nickel aluminide alloys with tungsten and molybdenum Carbides. *Inorg. Mater.* **2017**, *53*, 160–163. [CrossRef]
23. Pöttgen, R.; Jöhrendt, D. *Intermetallics: Synthesis, Structure, Function*; De Gruyter Textbook Oldenbourg: Berlin, Germany, 2014.
24. Lopatin, S.; Saji, I.; Viswanathan, S. *Molybdenum and Its Compounds: Applications, Electrochemical Properties and Geological Implications, Chemistry Research and Applications*; Nova Science Publishers, Inc.: Hauppauge, NY, USA, 2014.
25. Considine, G.D. *Van Nostrand's Encyclopedia of Chemistry*, 5th ed.; Wiley-Inter Science: New York, NY, USA, 2005; pp. 1038–1040. ISBN 978-0-471-61525-5.
26. Morales, E.R. Hydrogen Reduction Route towards the Production of Nano-Grained Alloys. Synthesis and Characterization of Fe<sub>2</sub>Mo Powder. Ph.D. Thesis, Institutionen för Materialvetenskap, KTH, Stockholm, Sweden, 2002. Available online: <http://kth.diva-portal.org/smash/get/diva2:9200/FULLTEXT01.pdf> (accessed on 20 February 2023).
27. Mazumder, S.; Pantawane, M.V.; Joshi, S.S.; Dahotre, N.B. Electrochemical and thermal-induced degradation of additively manufactured titanium alloys: A review. *Crit. Rev. Solid State Mater. Sci.* **2022**, *47*, 915–954. [CrossRef]
28. Boey, F.Y.C.; Khor, K.A.; Srivatsan, T.S.; Wang, M.; Zhou, W. *Processing and Fabrication of Advanced Materials VIII, Proceedings of a Symposium Organized by School of Mechanical & Production Engineering, Nanyang Technological University, Singapore, Singapore, 8–10 September 1999*; World Scientific Publishing: Singapore, 1999.
29. Abel Halim, K.S.; El-Geassy, A.A.; Ramadan, M.; Nasr, M.I.; Hussein, A.; Fathy, N.; Alghamdi, A.S. Reduction Behavior and Characteristics of Metal Oxides in the Nanoscale. *Metals* **2022**, *12*, 2182. [CrossRef]
30. Qu, Y.; Xing, L.; Shao, L.; Luo, Y.; Zou, Z. Microstructural characterization and gas-solid reduction kinetics of iron ore fines at high temperature. *Powder Technol.* **2019**, *355*, 26–36. [CrossRef]
31. Xing, L.Y.; Zou, Z.S.; Qu, Y.X.; Shao, L.; Zou, J.Q. Gas-Solid Reduction Behavior of In-flight Fine Hematite Ore Particles by Hydrogen. *Steel Res. Int.* **2019**, *90*, 1800311. [CrossRef]
32. Sohn, H.Y. Suspension Ironmaking Technology with Greatly Reduced Energy Requirement and CO<sub>2</sub> Emissions. *Steel Times Int.* **2007**, *31*, 68–72.
33. Abdel Halim, K.S.; Nasr, M.I.; El-Geassy, A.A. Developed model for reduction mechanism of iron ore pellets under load. *Ironmak. Steelmak.* **2011**, *38*, 189–196. [CrossRef]
34. El-Geassy, A.A.; Abdel Halim, K.S.; Bahgat, M.; Mousa, E.A.; El-Shereafy, E.E.; El-Tawil, A.A. Carbothermic reduction of Fe<sub>2</sub>O<sub>3</sub>/C compacts: Comparative approach to kinetics and mechanism. *Ironmak. Steelmak.* **2013**, *40*, 534–544. [CrossRef]
35. Cavus, H.; Kahruman, C.; Yusufoglu, I. Thermal decomposition kinetics of the thermal decomposition product of ammonium heptamolybdate tetrahydrate in air and inert gas atmospheres. In *T.T Chen Hoonary Symposium on Hydrometallurgy, Electrometallurgy and Materials Characterization*; TMS: Pittsburgh, PA, USA, 2012; pp. 785–796.
36. Kovács, T.N.; Hunyadi, D.; de Lucena, A.L.A.; Szilágyi, I.M. Thermal decomposition of ammonium molybdates. *J. Therm. Anal. Calorim.* **2016**, *124*, 1013–1021. [CrossRef]
37. Thomazeau, C.; Martin, V.; Afanasiev, P. Effect of support on the thermal decomposition of (NH<sub>4</sub>)<sub>6</sub>Mo<sub>7</sub>O<sub>24</sub>·4H<sub>2</sub>O in the inert gas atmosphere. *Appl. Catal. A Gen.* **2000**, *199*, 61–72. [CrossRef]

38. Laidler, K.J. The development of the Arrhenius equation. *J. Chem. Educ.* **1984**, *61*, 494. [[CrossRef](#)]
39. Sohn, H.Y.; Szekely, J. A Structural Model for Gas-Solid Reactions with a Moving Boundary-III. A Generalized Dimensionless Representation of the Irreversible Reaction between a Porous Solid and a Reactant Gas. *Chem. Eng. Sci.* **1972**, *27*, 763. [[CrossRef](#)]

**Disclaimer/Publisher's Note:** The statements, opinions and data contained in all publications are solely those of the individual author(s) and contributor(s) and not of MDPI and/or the editor(s). MDPI and/or the editor(s) disclaim responsibility for any injury to people or property resulting from any ideas, methods, instructions or products referred to in the content.